

Energy Advances

Accepted Manuscript

This article can be cited before page numbers have been issued, to do this please use: A. Suryaprakash, A. Ramar, F. M. Wang, K. W. Guji, C. D. D. Sundari and L. Merinda, *Energy Adv.*, 2024, DOI: 10.1039/D4YA00331D.



This is an Accepted Manuscript, which has been through the Royal Society of Chemistry peer review process and has been accepted for publication.

Accepted Manuscripts are published online shortly after acceptance, before technical editing, formatting and proof reading. Using this free service, authors can make their results available to the community, in citable form, before we publish the edited article. We will replace this Accepted Manuscript with the edited and formatted Advance Article as soon as it is available.

You can find more information about Accepted Manuscripts in the [Information for Authors](#).

Please note that technical editing may introduce minor changes to the text and/or graphics, which may alter content. The journal's standard [Terms & Conditions](#) and the [Ethical guidelines](#) still apply. In no event shall the Royal Society of Chemistry be held responsible for any errors or omissions in this Accepted Manuscript or any consequences arising from the use of any information it contains.

1

2 **Tautomerism and Nucleophilic Addition Influenced Performance**

3 **on Aqueous Organic Redox Flow Batteries of Chelidamic Acid**

4 **and Chelidonic Acid**

5

6 Surya Prakash,^a Alagar Ramar,^a Fu-Ming Wang,^{a,b,c,d,*} Kefyalew Wagari Guji,^a Citra Deliana

7 Dewi Sundari,^e and Laurien Merinda^a

8

9 ^aGraduate Institute of Applied Science and Technology, National Taiwan University of Science

10 and Technology, No.43, Sec. 4, Keelung Road, Taipei 106, Taiwan, R.O.C.

11 ^bR&D Center for Membrane Technology, Chung Yuan Christian University, Taoyuan, Taiwan

12 ^cSustainable Energy Center, National Taiwan University of Science and Technology, Taipei,

13 Taiwan

14 ^dDepartment of Chemical Engineering, Chung Yuan Christian University, Taoyuan, Taiwan

15 ^eDepartment of Chemistry Education, UIN Sunan Gunung Djati Bandung, Bandung, Indonesia

16

17 *Corresponding author, TEL: +886 2 27303755; FAX: +886 2 27303733 (Prof. Fu-Ming

18 Wang)

19 E-mail address: mccabe@mail.ntust.edu.tw (Prof. Fu-Ming Wang)

20

21

22

23

24

25

26

27

28



1
2
3
4
5
6
7
8
9
10
11
12
13
14
15
16
17
18
19
20
21
22
23
24
25
26

Abstract

The redox flow battery is a cost-effective solution for grid-scale energy storage. Its special feature of separate reservoirs and electrodes makes it easy to adjust electrolyte volume and electrode size, improving safety and scalability. In this work, we explore two organic anolytes, chelidamic acid (CDA) and chelidonic acid (CDO), which share similar molecular weight but differ in their heteroatoms: pyridone and pyrone. The half-cell potentials of CDA and CDO anolytes enable them to exhibit theoretical cell voltages of 0.49 V and 0.48 V, respectively, when coupled with $K_4[Fe^{II}(CN)_6]$ catholyte. CDA demonstrated a stable discharge capacity of 650 mAh/L over 17 days in a basic medium without any degradation. In contrast, CDO gradually loses its capacity over successive cycles. The mechanism for the decomposition of CDO was analysed through cyclic voltammetry, 1H -NMR, and FTIR spectroscopy techniques. The analytical results revealed that there was a significant impact of tautomerization in CDA and nucleophilic addition in CDO on the performance in ARFB.



1 Introduction

2 The global demand for energy increases significantly every decade due to the overpopulation
3 and economic growth. This is driven by the depletion of highly consumptive non-renewable
4 energy sources such as coal, oil, and gas. Numerous researchers are striving to provide
5 sustainable energy solutions by expanding renewable sources like solar and wind. However,
6 the intermittent nature of these sources poses challenges in storing and transporting large
7 amounts of energy to end-users. In recent years, the redox flow battery has shown remarkable
8 growth surpassing the Li-ion battery, attracting researchers due to its environmentally friendly
9 nature, cost-effectiveness, and high endurance.^{1, 2} Moreover, the redox flow battery offer
10 scalability and adaptability through the flexibility to adjust volume and electrode area to
11 precisely meet the requirements of consumers. Various types of redox systems have been
12 introduced, including all-vanadium, Zn/Br, and Fe/Cr. However, some inorganic materials face
13 challenges such as corrosive electrolytes, high costs, toxic materials, and low conductivity
14 solvents.³ To overcome these hurdles, researchers have turned to aqueous organic redox-active
15 materials as they use highly conductive solvents like water. In addition, these materials are
16 low-cost, offer safety, and use less corrosive supporting electrolytes such as KOH. For instance,
17 quinone, extracted from coal and wood tar, has been successfully used as an anolyte active
18 material in Quino energy.⁴ While various electrolytes like phenazine,¹ alloxazine,⁵ and flavin
19 ^{6, 7} have been explored, only a few meet the criteria for stability, solubility, capacity, and power
20 density. Enhancing material performance in commercial electrolytes has been accomplished
21 by two primary approaches. Firstly, structural chemistry is modified to improve potential,
22 solubility, and stability. Secondly, pH adjustments, electrochemical regeneration, and
23 modifications in the potential window are implemented to overcome degradation mechanisms
24 or side reactions of electrolytes, ensuring successive stability.^{2, 6-8}

25 Bo Yang et al. identified a voltage drop of 150 mV in the anthraquinone-2,6-disulfonic acid-
26 4,5-dihydroxybenzene-1,3-disulfonic acid aqueous redox flow battery (ARFB) after the first
27 few cycles which was attributed to Michael addition reactions to form additional hydroxy
28 substitutions on the benzene.⁹ In 2017, Sanford, et al, reported that low-potential pyridinium
29 anolyte degrades in a neutral solution (NaCl) due to catalytic proton reduction.⁸ In 2023, Grey
30 et al. reported an FMN/ $K_4[Fe^{II}(CN)_6]$ ARFB where hydrolysis products of 4-(D-ribo-2,3,4-
31 trihydroxypentyl-5'-phosphate)-3-oxo-3,4-dihydroquinoxaline-2-carboxylate under basic
32 condition caused a change in the charge plateau without loss in the voltage.⁷ Additionally, in
33 2022, the degradation of 2,6 dihydroxy androne (DHAQ) to DHA(L)²⁻ (double charging



1 plateau) was identified via in situ $^1\text{H-NMR}$, with subsequent electrochemical regeneration back
2 to DHAQ $^{2-}$.⁶ Furthermore, the discovery of tautomerization in 2,3-dimethylquinoxaline-6-
3 carboxylic acid via Bayesian inference coupled with density functional theory (DFT) analysis
4 provides valuable insights for filtering and selecting appropriate electrolytes for ARFB.²

5 Chelidamic acid (dihydro-4-oxo-2, 6-pyridone-dicarboxylic acid) and chelidonic acid (4-oxo-
6 4H-pyran-2, 6-dicarboxylic acid) are renowned for their ability to form stable organic
7 complexes or dimeric with various metals including vanadium, copper, and calcium.¹⁰⁻¹²
8 Furthermore, CDA has been utilized as an additive in the catholyte of vanadium-based ARFB.
9 ¹³ Recent research in 2020 revealed that dipicolinic acid, similar structure with CDA, serves as
10 an effective ligand when paired with chromium in a neutral redox flow battery, demonstrating
11 a solubility of 0.7 M and consistent performance over 120 cycles.¹⁴

12 The present work investigates two redox-active materials, chelidamic acid (CDA) and
13 chelidonic acid (CDO), as anolytes in an aqueous redox flow battery under alkaline conditions.
14 Despite their comparable molecular weights, they were subtly differentiated by the presence of
15 distinct heteroatoms, specifically the structure of pyridone and pyrone. Both are fully
16 conjugated aromatic compounds with carbonyl groups in their six-membered rings. Compared
17 to pyridone, pyrone possess a higher electron withdrawing characteristic due to the presence of
18 oxygen hetero atom. Generally, structures containing carbonyl groups have great potential in
19 energy storage applications.^{4,9,15} Compounds like CDA and CDO, which features two-electron
20 withdrawing group (-COOH), significantly impact solubility in aqueous media.^{2,16} Previously,
21 these materials were optimized as composite anode materials for Li-ion energy storage devices,
22 showing remarkable capacities of 740.2 mAh/g (CDA) and 562.8 mAh/g (CDO) over 250
23 cycles without capacity degradation.¹⁷ Given their promising performance in Li-ion anode
24 materials, CDA and CDO were chosen as redox-active anolytes in ARFB. The impact of
25 heteroatoms in CDA and CDO was investigated by constructing ARFB with potassium
26 hexacyanoferrate (II) trihydrate. Additionally, our investigation reveals novel insights into
27 nucleophilic addition at α , β unsaturated carbon (CDO), as evidenced by FTIR and $^1\text{H-NMR}$
28 analysis. Furthermore, CDA demonstrates stable charge-discharge behaviour, underscoring the
29 impact of tautomerism in alkaline ARFB.

30

31 Experimental procedure



1 **Materials and Characterisation**

2 Potassium hydroxide (KOH, molecular weight: 56.11 g/mol, purity: 85%), potassium
3 hexacyanoferrate (II) trihydrate ($K_4[Fe^{II}(CN)_6] \cdot 3H_2O$, molecular weight: 422.39 g/mol, purity:
4 98.5%), chelidamic acid hydrate (CDA, molecular weight: 183.12 g/mol, purity: $\geq 97\%$), and
5 chelidonic acid (CDO, molecular weight: 184.10 g/mol, purity: 97%) were purchased from
6 Sigma Aldrich, Merck Limited, Taiwan. Deuterium Oxide (D_2O , molecular weight: 20.027
7 g/mol, purity: 99.8% D) was purchased from Thermo Scientific Chemicals. The Sustainion X-
8 37 FA membrane was obtained from Dioxide Materials, a CO_2 recycling company. Carbon felt
9 (thickness – 6.5 mm) was purchased from clean energy technology. BioLogic VMP3
10 multichannel Potentiostat was employed for electrochemical measurements, while SP-150e
11 was used for ARFB testing. Bruker AVANCE III HD 600 MHz nuclear magnetic resonance
12 (NMR) spectrometer was utilized for 1H -NMR analysis. UV-visible analysis in the range of
13 190 to 800 nm was conducted using a V-670 JASCO spectrometer. FT/IR – 6700, JASCO
14 Fourier transform infrared spectroscopy (FTIR) was performed with powdered samples in the
15 range of $4000 - 400\text{ cm}^{-1}$. Pin flow energy storage devices were employed in this study.

16 **Solubility test**

17 CDA and CDO were added in 5 ml of 1 M KOH solution until saturation was achieved. The
18 solution was left overnight, and then filtration was used to eliminate insoluble residues. The
19 soluble anolyte obtained was diluted to lower concentrations to compare it against known
20 concentration standards. This process helps to determine the maximum solubility of both CDA
21 and CDO.

22 **Electrochemical measurement**

23 Cyclic voltammetry (CV) and linear sweep voltammetry (LSV) were measured by using three-
24 electrode system in a closed environment at 25 °C. A three-electrode system consisting of
25 glassy carbon (with an active surface area - 0.196 cm^2) as a working electrode, a platinum wire
26 (99.99%) as a counter electrode, and an Ag/AgCl electrode soaked in a 3 M AgCl solution
27 serving as a reference electrode was employed to perform CV and LSV measurements. Before
28 each measurement, the glassy carbon electrode surface was polished using alumina suspension
29 and then sonicated for 3 minutes, followed by cleaning with ethanol. Electrochemical
30 characterizations were performed using a BioLogic VMP3 multichannel Potentiostat. A 5 mM
31 of CDO and CDA dissolved in 1 M KOH was employed, with a scan rate of 10 mV/s. LSV



1 measurement was carried out by a rotating disc electrode (RDE) fixed with a Pine rotating
2 shaft. A 5 mM of CDO/CDA dissolved in 1 M KOH was tested at various rotation speeds from
3 300 – 2700 rpm, with a potential sweep value of 10 mV/s, from 0 to -0.6 V. LSV measurements
4 of 5 mM of $K_4[Fe^{II}(CN)_6]$ in 1 M KOH were carried out in the potential range from 0 to 0.6
5 V.

6 Redox flow battery tests

7 The anolyte and catholyte were prepared in a ratio of 1:2, due to the quasi-reversible nature of
8 CDO and CDA. A solution containing 50 mM of CDA or CDO with 100 mM of $K_4[Fe^{II}(CN)_6]$
9] dissolved in 1 M KOH was used. The flow of the electrolyte was controlled at 25 rpm using
10 a peristaltic pump via the flow-by method.¹⁸ To enhance the wettability of the carbon felt
11 (active surface area – 5 cm²), it was sintered for 12 hrs at a stable temperature of 400 °C in a
12 high-temperature furnace before assembling a battery. This process increased the
13 electrochemical surface area of the carbon felt, improving its contact with the electrolyte. An
14 imidazolium-functionalized styrene and vinyl benzyl chloride polymer membrane (X-37 FA
15 membrane) was used as an anion exchange membrane to separate the anolyte and catholyte.
16 The membrane was immersed in 1 M KOH to convert Cl⁻ ions into OH⁻ ions, making it
17 suitable for use in an ARFB. After assembling the battery, a potentiostat SP-150e was used to
18 apply a constant current of 0.4 mA/cm² and monitor the performance of the ARFB.

19 Computational Method

20 Geometry optimizations and single point frequency calculations for all structures were
21 conducted in Orca 4.2.0 software package. The initial structures of chelidamic acid (CDA) and
22 chelidonic acid (CDO) was constructed using Avogadro software. Density functional theory
23 (DFT) calculations were performed using with B3LYP hybrid functional and 6-311++G(d,p)
24 basis set. Spin-unrestricted calculations are used to allow for any possible bond cleavage during
25 geometry optimization of the radical species. The solvent effect was included in the
26 calculations by employing the conductor-like polarizable continuum model (CPCM), using a
27 dielectric constant of 70, to implicitly account for solvent effects of 1 M KOH. The optimized
28 molecular geometries and HOMO-LUMO isosurfaces were visualized using Chemcraft.

29

30

31



1 Result and discussion

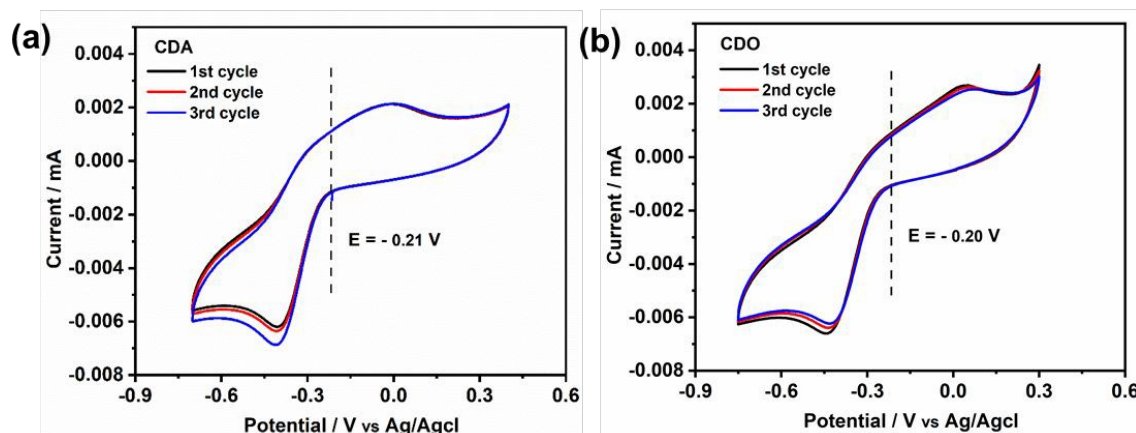
2 Electrochemical characterization

3 The cyclic voltammetry measurements were performed to determine the standard potential of
4 redox active material. Additionally, the reversibility was assessed by evaluating the ratio of
5 peak current between the anodic and cathodic. The value of ratio 1 indicates a reversible
6 electrochemical reaction ($\frac{I_{pa}}{I_{pc}} = 1$). In our study, the initial three cycles of CDO and CDA were
7 analyzed, revealing a quasi-reversible ($\frac{I_{pa}}{I_{pc}} \neq 1$) rate of electron transfer rate between the
8 electrode and the redox material, as indicated by the unequal peak current values of I_{pa} and I_{pc}
9 in the negative potential range.¹⁹ The standard redox potential of CDA and CDO were
10 calculated from the anodic and cathodic peak potential ($(E_{pa} + E_{pc})/2$), yielding values of –
11 0.21 and – 0.20 V vs Ag/AgCl, respectively (Fig.1). In both cases, the ketone served as the
12 active site for the electrochemical reduction, similar to quinone, and anthraquinone in Fig.2.¹⁵
13 The reduction behavior of CDA (pyridone) is evident in compounds like benzo[g]quinoline-
14 4,5,10(1H)-trione, which contains a pyridone substructure. This reduction is observed when
15 the compound is dissolved in DMSO (dimethyl sulfoxide).²⁰ The reduction behavior of CDO
16 is demonstrated in the xanthone structure, where the carbonyl group (C=O) is reduced by
17 hydride (H-) transfer, resulting in the formation of a hydroxyl radical (C-OH). In this process,
18 the pyrone ring acts as the redox center.²¹ When coupled with $K_4[Fe^{II}(CN)_6]$ as a redox-
19 active organo-metallic catholyte, CDA and CDO exhibited a theoretical potential window of
20 0.49 and 0.48 V, respectively.

21 To demonstrate the reversibility of CDA and CDO, a long-term cyclability test was conducted
22 using cyclic voltammetry, as shown in Fig. S1. Over 100 cycles, CDA exhibited more stable
23 cyclic reversibility compared to CDO. In the case of CDA, the observed increase in reduction
24 current and the shift with the number of cycles may be attributed to the deposition of CDA on
25 the glassy carbon electrode surface, facilitated by the contact of the amine group.^{22, 23} This
26 organic molecule deposition increases capacitance, which in turn leads to a higher reduction
27 current as the number of cycles increases, a finding supported by previous research.²⁴
28 Additionally, chelidamic acid forms polymeric or dimeric structures with metal ions and
29 hydrogen bonds with water, creating water clusters. This phenomenon, reported in previous
30 research, provides evidence for the rise in reduction current as the number of cycles increases.²⁵



- 1 In contrast, due to low conjugation, CDO undergoes irreversible within a few cycles, leading
 2 to a decrease in current and a loss of reversibility as the number of cycles increases.



3
 4 Fig. 1 Cyclic voltammetry of 5 mM of (a) CDA and (b) CDO at the scan rate of 10 mV/s in 1
 5 M KOH supporting solution.

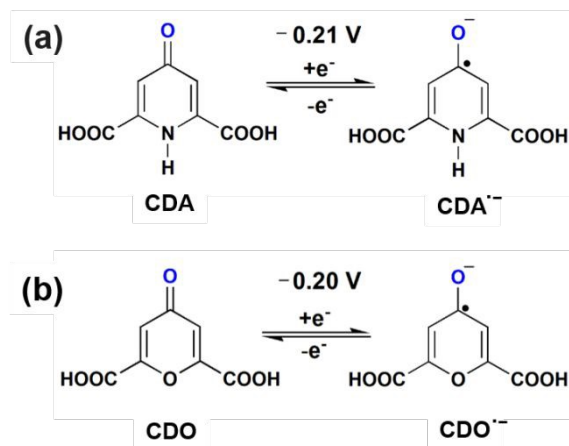
6 In LSV measurements (Fig. 3a-b, S2a), the limiting current value elucidates the transition of
 7 active material from a stable state to a charged state.⁹ This transition results in a limiting current
 8 (i_L) that varies with the square root of the angular velocity ($\omega^{1/2}$), as explained by the Levich
 9 equation (1)¹⁹. The observed linear inverse relationship between the limiting current decreases
 10 and the increase in rotation speed suggests that the electrochemical reduction was controlled
 11 by diffusion. The kinetics of diffused redox-active species are crucial for the optimal
 12 performance of redox flow batteries. Ensuring fast diffusion rates helps in achieving higher
 13 current densities and lower overpotentials, leading to more efficient and effective energy
 14 storage and delivery. The kinetic rate constant of the redox active materials was then calculated
 15 by using the diffusion coefficient value obtained from the equation (1), with the slope value of
 16 CDA, and CDO recorded as 1.7158×10^{-6} and 1.916×10^{-6} mA rad⁻¹ s⁻¹, from the Koutecky
 17 Levich plot (Fig. 3e, S2b),

$$18 \quad i_L = 0.625nFAD^{2/3}\omega^{1/2}\nu^{-1/6} C_0 \quad (1)$$

19 Where n represents the number of electrons involved in the electrochemical reaction (in this
 20 case, n = 1), F denotes Faraday's constant (96,485 C mol⁻¹), A represents the surface area of
 21 the electrode (0.196 cm²), D signifies the diffusion coefficient of the redox active material, ν
 22 denotes the kinetic viscosity of 1 M KOH (1.07×10^{-2} cm² s⁻¹) and C_0 represents the
 23 concentration of the active material (0.005×10^{-3} mol cm⁻³). Consequently, the diffusion



1 coefficient (D) values for CDA and CDO were calculated as 5.09×10^{-8} , and 5.998×10^{-8}
 2 $\text{cm}^2 \text{s}^{-1}$. To minimize error, the diffusion coefficient value of the known $K_4[Fe^{II}(CN)_6]$ was
 3 determined from Fig. S2 and compared with previously published research papers.^{15, 26}



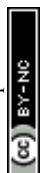
4
 5 Fig. 2 Electrochemical redox mechanism of (a) CDA and (b) CDO.

6
 7 In the Koutecky Levich plot, the inverse limiting current value ($1/i_L$) was plotted against the
 8 inverse square root of various overpotentials ($1/\omega^{1/2}$), showing a linear relationship (Fig. 3c-d,
 9 S2c). The logarithm of the kinetic current ($\log i_k$) value was extracted from the intercept of the
 10 y-axis (where $1/\omega^{1/2} = 0$) or it can be calculated from the equation (2). Additionally, the Tafel
 11 plot was plotted with various over potential against their corresponding $\log i_k$ values (Fig. 3f,
 12 S2d) and the antilogarithm of intercept (where the overpotential is zero) of the y-axis is equal
 13 to $nFAk_0C_0$, which is used to calculate the kinetic rate constant,^{19, 27, 28}

$$14 \quad \frac{1}{i} = \frac{1}{i_k} + \frac{1}{i_L} = \frac{1}{i_k} + \frac{1}{0.625nFAD\frac{2}{3}\omega^{1/2}\frac{-1}{6}C_0} \quad (2)$$

$$15 \quad i_k = nFAk_0C_0 \quad (3)$$

16 From equation (3), the calculated kinetic rate constant (k_0) for CDA, and CDO were found to
 17 be 2.66×10^{-4} , and $2.26 \times 10^{-4} \text{ cm s}^{-1}$, respectively (Table 1). The derived kinetic rate constant
 18 of $K_4[Fe^{II}(CN)_6]$ (Fig. S2) align well with those reported in the literature, indicating a high
 19 level of comparability.²⁹ However, it is noteworthy that the kinetic rate constant of CDA and
 20 CDO were larger than those of vanadium redox flow battery electrolytes such as V^{2+}/V^{3+} and
 21 VO^{2+}/VO_2^+ , which were reported as 1.75×10^{-5} and $7.5 \times 10^{-4} \text{ cm s}^{-1}$.^{30, 31} Additionally, the



1 CDA and CDO exhibited a maximum solubility of 0.55 M and 0.59 M in 1 M KOH, as
2 determined by UV–visible spectra (Fig. S3).

3

4 **Charge–discharge and Structural characterization**

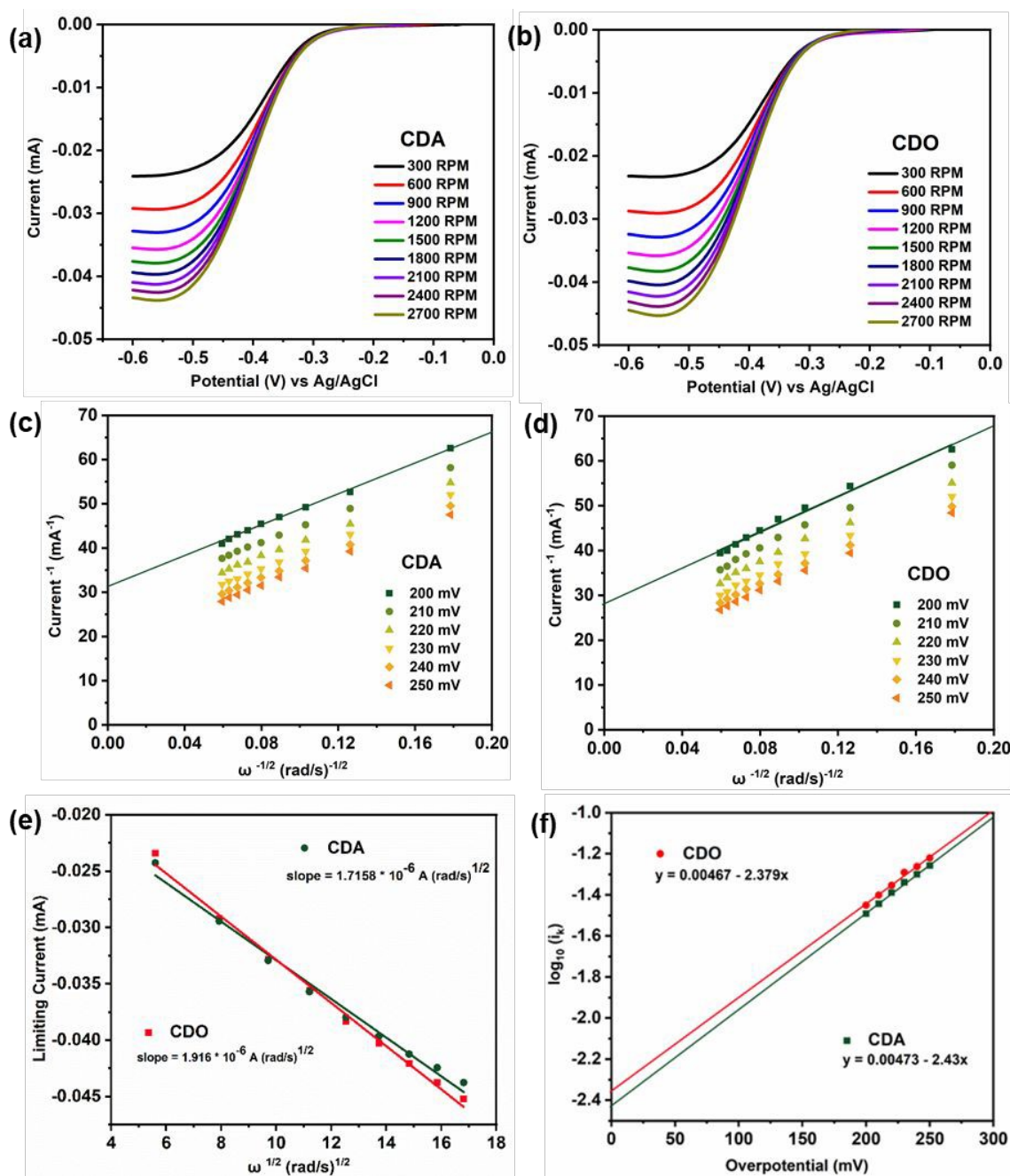
5 The ARFB of CDA/ $K_4[Fe^{II}(CN)_6]$ and CDO/ $K_4[Fe^{II}(CN)_6]$ underwent charge-discharge
6 cycles over 10 cycles within the voltage range of 0 to 0.9 V (Fig. 4(a, b)). Notably, the charge-
7 discharge characteristics of both CDA and CDO displayed an unusual charge-discharge plateau,
8 indicating their dependence on structural characteristics. The discharge capacity of CDA/ $K_4[Fe^{II}(CN)_6]$
9 started at approximately 630 mAh/L in the first cycle, gradually increasing to
10 around 650 mAh/L and remaining stable for up to 17 days. Conversely, CDO/ $K_4[Fe^{II}(CN)_6]$
11 displayed its discharge capacity approximately 880 mAh/L but linearly declined to 630 mAh/L
12 by the end of 21 days (Fig. 4c, d). This indicates that the pyridone heterocyclic compound in
13 CDA offers greater stability compared to the pyrone compound in CDO. Regarding the energy
14 efficiency (EE), coulombic efficiency (CE), and voltage efficiency (VE), CDA exhibited an
15 average values of 36 %, 87%, and 41%, respectively while CDO showed an average values of
16 19 %, 74 %, and 24 %, respectively (Fig. 4e, f).³² These outcomes suggest the superior
17 performance of CDA compared to CDO. The performance of redox flow batteries at low
18 current density often results in lower coulombic efficiency (CE) due to uneven ion and electron
19 transfer, unlike the more efficient charge transfer observed at higher current densities.
20 Additionally, the voltage window during charge-discharge testing also impacts coulombic
21 efficiency.³³

22 In the first cycle of CDA/ $K_4[Fe^{II}(CN)_6]$ and CDO/ $K_4[Fe^{II}(CN)_6]$, a single charge plateau
23 was observed alongside a corresponding discharge plateau. Interestingly, in this initial cycle,
24 the capacity of the charge plateau was three times higher than the discharge capacity, resulting
25 in a lower CE of approximately 20 % (Fig. 4c, d). The high Charge capacity in the first cycle
26 is related to the total electron withdrawal from the 0.1 M $K_4[Fe^{II}(CN)_6]$. However, the low
27 discharge capacity is linked to the limited reversible electron release process from CDA and
28 CDO. This discrepancy leads to low coulombic efficiency in the first cycle. However, from the
29 second cycle, the charging process exhibited two distinct plateaus, the first one at 0 V and the
30 next at approximately 0.7 V, while a single discharge plateau remained. Notably, these two
31 plateaus reversibly appeared from the second cycle to the tenth cycle in CDA, maintaining a



1 stable capacity. In contrast, in CDO, the voltage of the plateaus (~ 0.7 V) increases with each
 2 cycle, resulting in a decrease in both charge and discharge capacity.

3



4

5 Fig. 3 Linear sweep voltammetry of 5 mM of (a) CDA and (b) CDO at 10 mV/s scan rate in 1
 6 M KOH supporting electrolyte using RDE. Levich plot of (c) CDA and (d) CDO derived from
 7 (a, b). (e) Levich plot $\omega^{1/2}$ against limiting current to calculate the D value of CDA and CDO.
 8 (f) Tafel plot of CDA and CDO derived from (c, d).

9

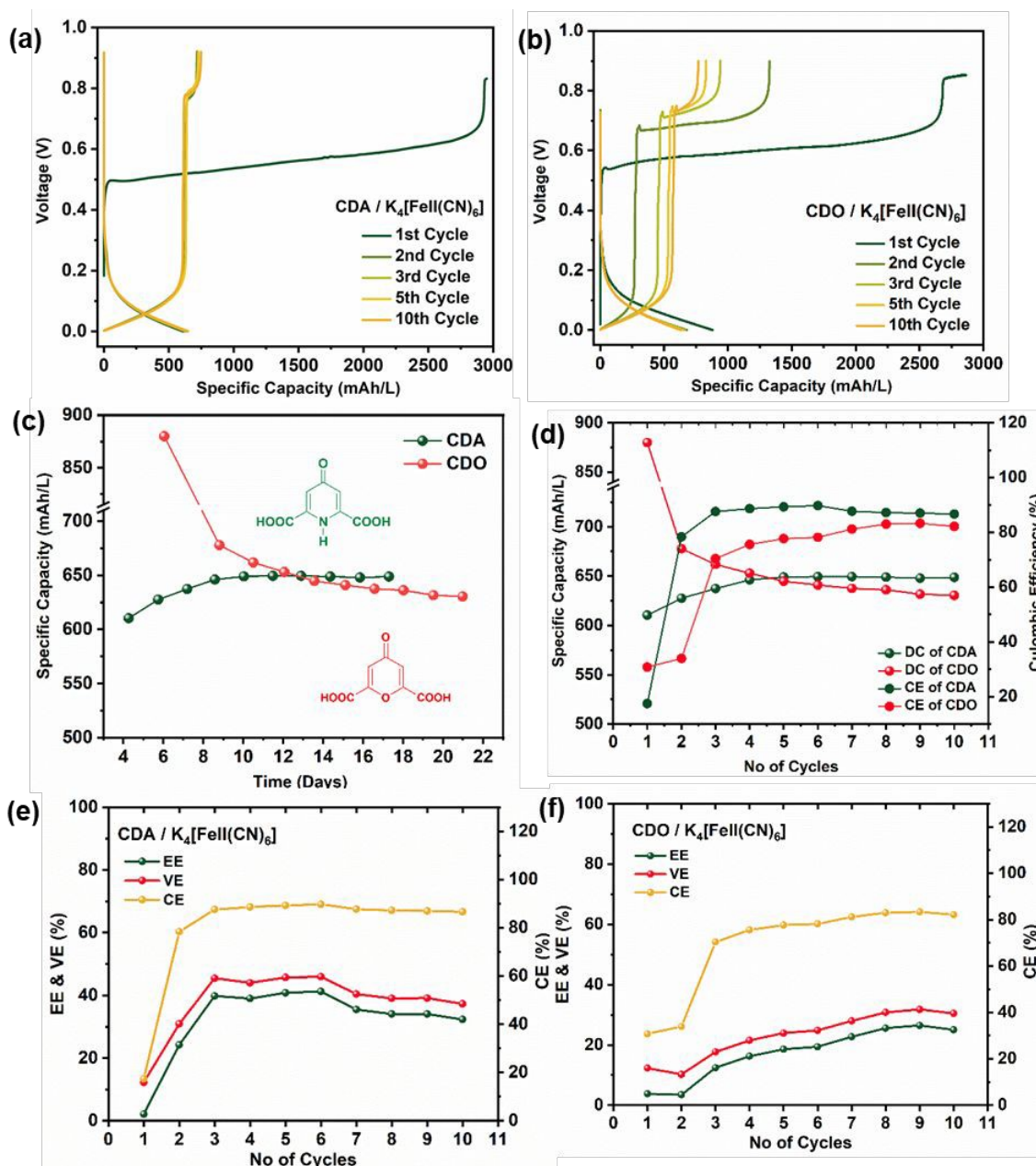


1

2 Table 1. shows the half-cell potential, diffusion coefficient, and kinetic rate constant of CDA,
3 and CDO.

Anolyte	Half-cell potential (V)	Diffusion coefficient ($\text{cm}^2 \text{s}^{-1}$)	Kinetic rate constant (cm s^{-1})
CDA	-0.21	5.09×10^{-8}	2.26×10^{-4}
CDO	-0.20	5.998×10^{-8}	2.66×10^{-4}

4

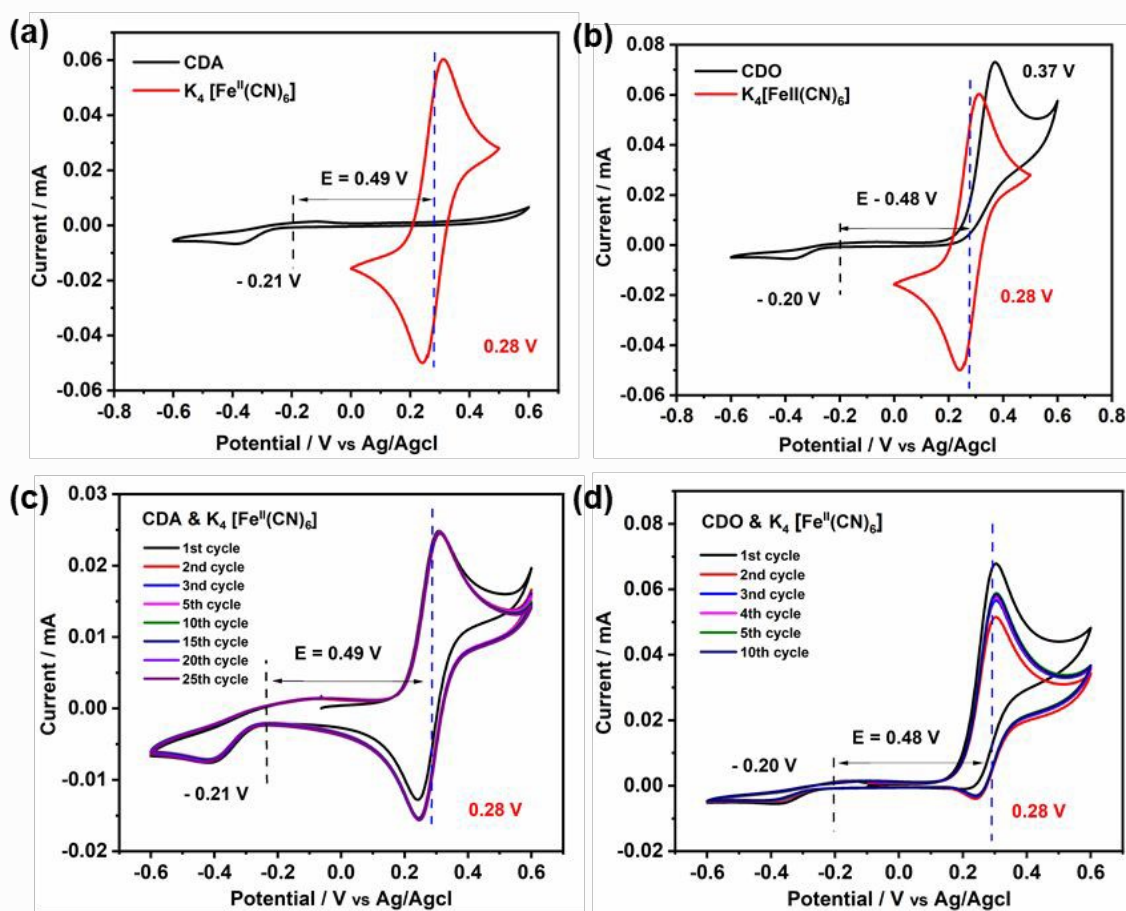


5

6 Fig. 4 shows the ARFB results of (a, b) charge-discharge profile of CDA and CDO (c) time vs
7 specific capacity of CDA and CDO (d) discharge capacity (DC) and CE of CDA and CDO vs
8 number of cycles (e, f) cycle number vs CE, EE, and VE of CDA and CDO.



1 X-37 FA membranes were subjected to FTIR analysis before and after 10 cycles of CDA/ $K_4[Fe^{II}(CN)_6]$
 2 $Fe^{II}(CN)_6$ and CDO/ $K_4[Fe^{II}(CN)_6]$ to assess their stability, which could potentially impact
 3 the voltage drop in the ARFB. The membrane primarily comprised tetra methyl imidazole
 4 along with a copolymer of styrene and vinyl benzyl chloride (VBC). The presence of O-H
 5 stretching at 3400 cm^{-1} indicated the OH group of KOH or $K_4[Fe^{II}(CN)_6]$, while the small
 6 peak at 2040 cm^{-1} denoted the $C\equiv N$ peak from the $K_4[Fe^{II}(CN)_6]$.^{30, 31} Additionally, peaks
 7 observed at 2923 , 2850 , and 3021 cm^{-1} represent the C-H (sp^3) and =C-H (sp^2) stretching of
 8 tetramethyl imidazole, as depicted in Fig. S4. Peaks at 1647 and 1561 cm^{-1} were attributed to
 9 the C=N or N=C-N stretching vibration of the imidazole ring structure.³⁴ The persistent
 10 appearance of the stretching bands of imidazole $C=N^+$ and $C-N^+$ at 1495 and 1445 cm^{-1} (Fig.
 11 3),³⁵ before and after 10 cycles suggests that the X-37 FA membrane was not associated with
 12 the emerging new plateau in the second cycle.



13

14 Fig. 5 Cyclic voltammetry of (a) 5 mM of CDA and $K_4[Fe^{II}(CN)_6]$ in 1 M KOH (b) CDO and
 15 $K_4[Fe^{II}(CN)_6]$ in 1 M KOH (c) equally mixed electrolyte of 5 mM of CDA and $K_4[Fe^{II}(CN)_6]$
 16] in 1 M KOH (d) CDO and $K_4[Fe^{II}(CN)_6]$ in 1 M KOH.



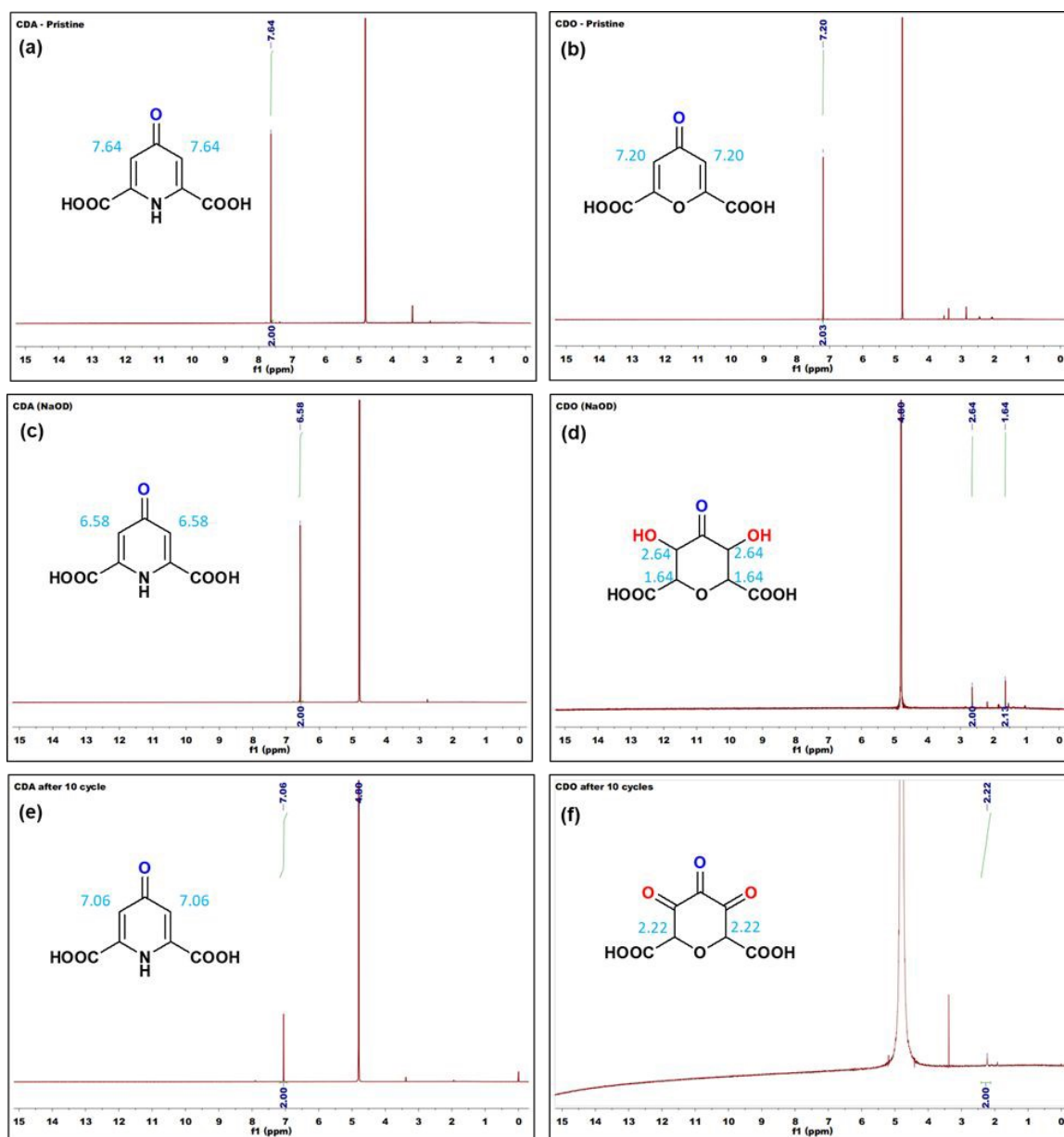
1
2
3
4
5
6
7
8
9
10
11
12
13
14
15
16
17
18
19
20
21
22
23
24
25
26
27
28
29
30

To understand the difference in stability between CDA and CDO, cyclic voltammetry measurements were conducted from -0.6 V to 0.6 V and compared with $K_4[Fe^{II}(CN)_6]$ (Fig. 5(a, b)). Notably, no peak appeared in the CDA within the positive potential range, whereas a significant oxidation peak appeared at 0.37 V in CDO, closely aligned with the oxidation peak of $K_4[Fe^{II}(CN)_6]$. This prompts curiosity about the compatibility of CDA and CDO analytes with $K_4[Fe^{II}(CN)_6]$ in basic solution, especially when cross-over occurs in ARFB. Consequently, an investigation was initiated to explore the cyclic voltammetry stability of the analyte when paired with an equal amount of catholyte.²⁷ The cyclic voltammetry of equimolar mixed CDA and $K_4[Fe^{II}(CN)_6]$ exhibited stable cyclic behavior over 25 cycles at a scan rate of 5 mV/s (Fig. 5c). However, employing the same approach with CDO revealed a quasi-reversible $K_4[Fe^{II}(CN)_6]$ cyclic behavior, accompanied by a reduction in current values with an increasing number of cycles (Fig. 5d). This observation sheds light on the reason for the notable loss of discharge capacity in CDO/ $K_4[Fe^{II}(CN)_6]$ systems. However, that doesn't explain the mechanism behind the unstable CDO in the basic medium.

In addition, to gain insight into the structural changes in CDA and CDO before and after reaction, ¹H-NMR spectroscopy was employed. As depicted in Fig. 6, the olefinic proton peaks of CDA and CDO (in D₂O solvent) were observed at 7.64 and 7.20 ppm (Fig. 6a, b), respectively. Upon dissolution of pristine CDA and CDO in a solution containing 40% NaOH + D₂O, their stability in basic conditions was varied. Interestingly, the absence of the proton peak at 7.20 ppm was noted in CDO, while the proton peaks of CDA shifted to 6.58 ppm due to the high molarity of 3 M NaOD.³⁶ The observed shift of the proton signal belonging to CDA indicates the occurrence of tautomerism in the basic medium (Fig. 6c).³⁷ Subsequent ¹H-NMR data of CDO after 10 cycles of discharge showed no peaks around 7 ppm. However, it is supported by the presence of proton peak at 2.22 ppm (Fig. 6f). The absence of a proton peak in CDO suggests a nucleophilic addition reaction in the basic medium, which is supported by the proton peaks at 2.64 and 1.64 ppm (Fig. 6d). However, CDA retained its proton peak at 7.06 ppm even after 10 cycles (Fig. 6e), indicating its stability in the basic medium over multiple cycles.



1



2

3 Fig. 6 $^1\text{H-NMR}$ spectra of (a) CDA in its pristine form (D_2O solvent) (c) pristine CDA in the
 4 solution of 40 % of NaOD + D_2O (e) CDA after 10 cycle (D_2O solvent) (b) CDO in its pristine
 5 form (D_2O solvent) (d) pristine CDO in the solution of 40 % of NaOD + D_2O (f) CDO after 10
 6 cycle (D_2O solvent).

7

8

9

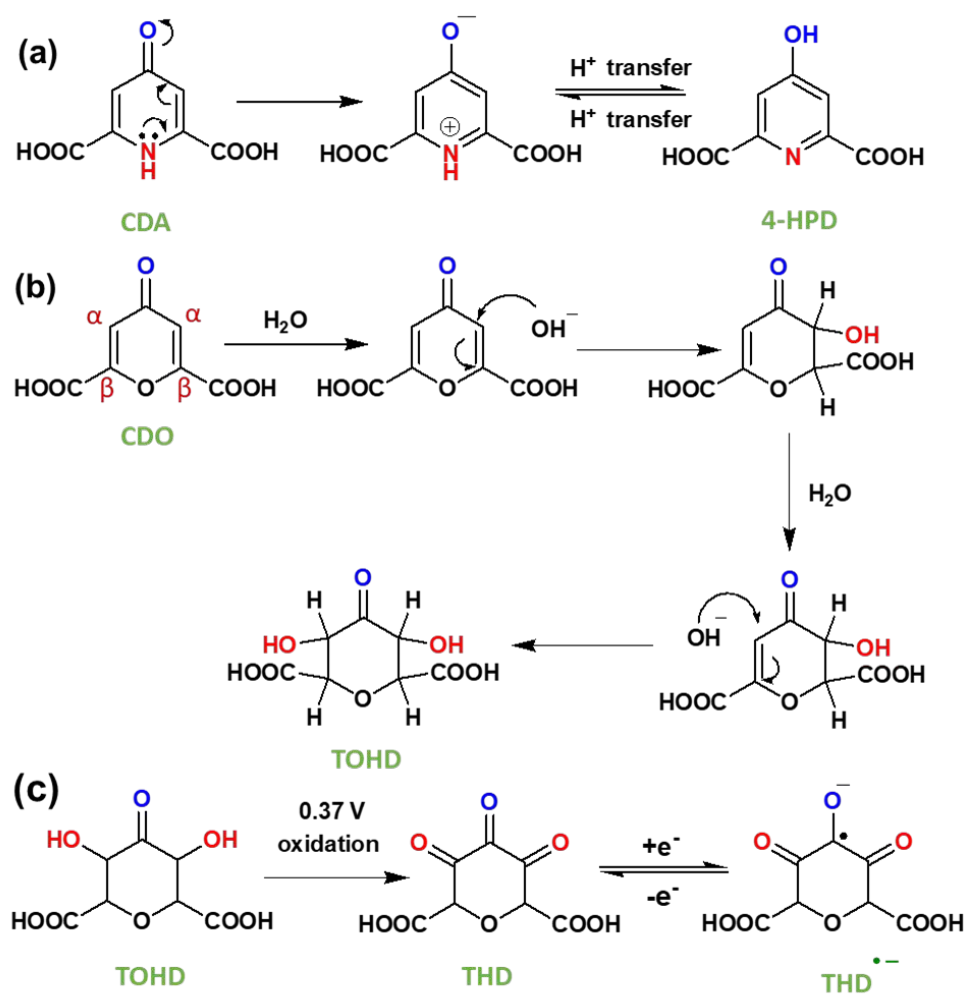


1 Tautomerization is a chemical reaction that results in the rearrangement of bonds in a
2 compound. This process creates an equilibrium between the keto form, characterized by a
3 carbon-oxygen double bond (C=O), and the enol form, which features a carbon-oxygen single
4 bond (C–OH). In CDA (Fig. 7a), tautomerization involves the shifting of a proton between
5 amine nitrogen to carbonyl oxygen, leading to keto (C=O) – enol (C–OH) tautomerization.
6 This process involves the conversion of dihydro-4-oxo-2, 6-pyridone-dicarboxylic acid (CDA)
7 into 4- hydroxy pyridone-2, 6-dicarboxylic acid (4-HPD).^{37, 38} In the RFB environment,
8 particularly in an alkaline solution, nucleophiles like H₂O and OH[–] are predominant. In CDO
9 (Fig. 7b), a carbon-carbon double bond is located adjacent to an α , β -unsaturated ketone
10 (carbonyl ketone). The carbon atom directly attached to the carbonyl group is known as the α
11 carbon, followed by the β carbon. The electron-withdrawing nature of the carbonyl group make
12 this double bond is highly reactive towards nucleophiles (–OH) in an alkaline medium. The
13 nucleophiles directly add to the α carbon, forming a saturated ketone (carbonyl ketone) as
14 shown in Fig. 7b.^{39, 40} This process involves the conversion of 4-oxo-4H-pyran-2,6-
15 dicarboxylic acid (CDO) into tetrahydro-3,5-dihydroxy-4-oxo-2H-pyran-2,6-dicarboxylic acid
16 (TOHD). The structure of TOHD is further supported by the ¹H-NMR spectra in Fig. 6d (CDO-
17 NaOD). In Fig. 7c, the presence of Tetrahydro-3,4,5-trioxo-2H-pyran-2,6-dicarboxylic acid
18 (THD) is evidenced by an oxidation peak at 0.37 V in the cyclic voltammetry (Fig. 5b). These
19 oxidation behaviours have been previously reported in quinoxaline derivatives in the alkaline
20 medium.⁴¹ Furthermore, the presence of THD is confirmed by the ¹H-NMR spectra of CDO
21 after 10 cycles of discharge, as shown in Fig. 6d. These finding helps to support the
22 tautomerization and nucleophilic addition reaction in CDA and CDO in Fig. 7.

View Article Online
DOI: 10.1039/D4YA00331D



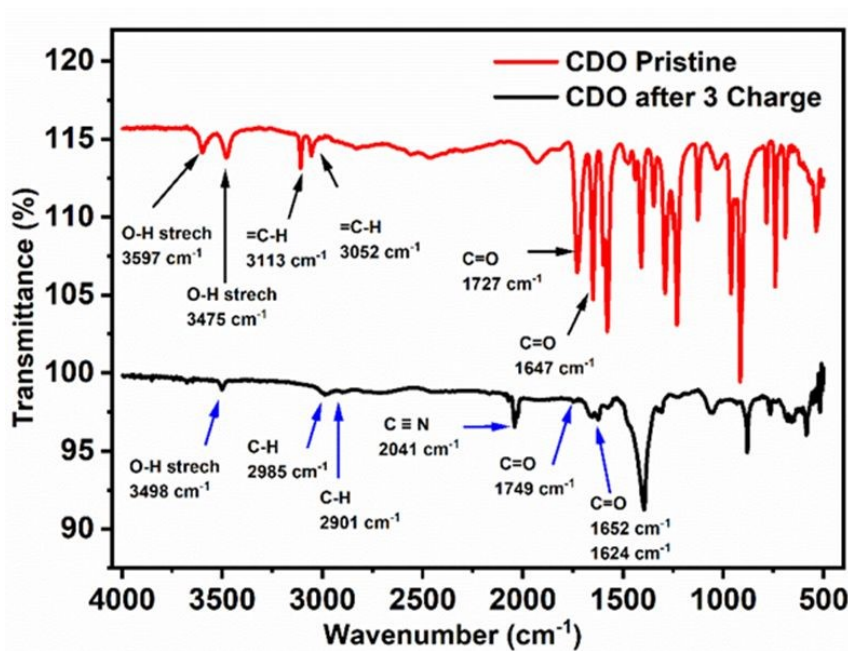
1



2

3 Fig. 7 (a) Tautomerization reaction mechanism in CDA (b) nucleophilic addition mechanism
4 in CDO (c) electrochemical reaction in CDO after nucleophilic addition.

 Open Access Article. Published on 05 sentyabr 2024. Downloaded on 11.09.2024 00:28:10.
 This article is licensed under a Creative Commons Attribution-NonCommercial 3.0 Unported Licence.

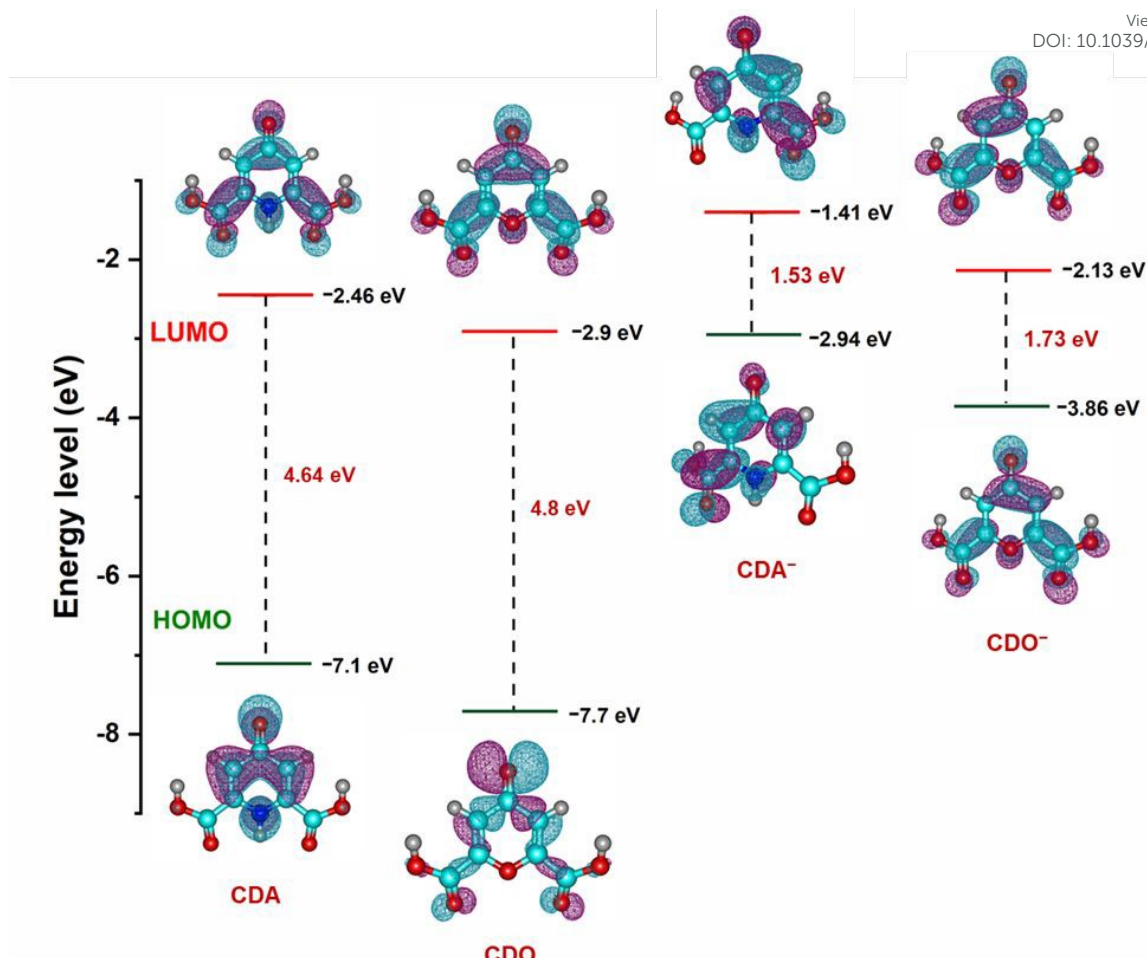
View Article Online
DOI: 10.1039/D4YA00331D

Fig. 8 FTIR spectra of Pristine CDO and after 3 charges of CDO.

To further confirm the nucleophilic addition to CDO, FTIR spectra of pristine and after three charge cycles of electrolyte samples were obtained. In pristine CDO (Fig. 8), the O-H stretching was observed at 3597 and 3475 cm^{-1} , corresponding to the $-\text{COOH}$ group, while the $=\text{C}-\text{H}$ (sp^2) modes of CDO were noted at 3113 and 3052 cm^{-1} . The $\text{C}=\text{O}$ conjugated functional group was located at 1727 cm^{-1} , indicating the $-\text{COOH}$, and the $\text{C}=\text{O}$ redox-active site was found at 1647 cm^{-1} .

After three charge cycles of CDO, a peak shift of the O-H stretch was observed at 1498 cm^{-1} , transition from $=\text{C}-\text{H}$ (sp^2) to $-\text{C}-\text{H}$ (sp^3).^{17, 42} Additionally, the peak at 2040 cm^{-1} represents the $\text{C}\equiv\text{N}$ peak from $\text{K}_4[\text{Fe}^{\text{II}}(\text{CN})_6]$, which denotes cross-over in the battery.³¹ The $\text{C}=\text{O}$ stretching of $-\text{COOH}$ shifts to 1749 cm^{-1} due to the reduced conjugation in CDO. Notably, the presence of two carbonyl peaks at 1652 and 1623 cm^{-1} provides evidence of two hydroxyl groups or nucleophilic additions after the first cycle. This is further supported by the absence of the proton peak in 40% $\text{NaOH} + \text{D}_2\text{O}$ and after ten cycles, as observed in the ^1H -NMR of CDO, along with the presence of an oxidation peak in CV.⁴³





1
2 Fig. 9 Optimized structure and calculated energy levels of CDA, CDO and charged CDA⁻,
3 CDO⁻ from DFT simulations.

4 The nucleophilic addition at α , β – unsaturated carbon (concerning carboxylic acid) not only
5 explains the loss of discharge capacity but also accounts for the appearance of a new plateau
6 in CDO after the first cycle in an alkaline medium. In contrast, the stability of CDA in the basic
7 medium is attributed to tautomerism. Simply, tautomerism in CDA refers to the transfer of a
8 proton from amine nitrogen to carbonyl oxygen. Due to this proton transfer in CDA,
9 nucleophilic addition predominantly does not occur at the pyridone heteroatoms. As a result of
10 enaol-1 reduction, two stable charge plateaus appear over 10 cycles (17 days).¹¹ Additionally,
11 the performance of a high concentration ARFB with 0.4 M CDA and CDO analysed using a
12 current density of 40 mA/cm², is shown in Fig. S5 and S6. CDA demonstrates stable cyclic
13 performance over 230 cycles, significantly outperforming CDO at high current density, with
14 an average coulombic efficiency of 98%. This observation suggests that CDA exhibits better
15 performance in ARFB compared to CDO in a basic medium.



1
2 To further support the finding on electrolyte stability and conductivity, the highest occupied
3 molecular orbital (HOMO) and lowest unoccupied molecular orbital (LUMO) value of CDA,
4 CDO, and their charged forms (CDA⁻ and CDO⁻) were calculated using DFT analysis, as
5 shown in Fig. 9. The energy gaps of CDA, CDO, CDA⁻ and CDO⁻ are 4.64, 4.8, 1.53 and
6 1.73eV, respectively. According to frontier molecular orbital analysis, molecule with small
7 energy gap tend to exhibit greater electrolyte stability and higher conductivity. The smaller
8 energy gap in CDA and CDA⁻ anion compared to CDO and CDO⁻ suggest that CDA is more
9 stable than CDO. Additionally, the DFT analysis of the molecular charge distribution for CDA,
10 CDO, 4-HPD⁻, and THD⁻, as shown in Fig S7, provides further insights into their molecular
11 reactivity. The analysis highlights regions of negative (blue) and positive (green) charges,
12 which indicate potential sites for nucleophilic and electrophilic reactions. In CDA, CDO, and
13 THD⁻, a significant negative charge is concentrated on the carbonyl group at the 4-position,
14 suggesting this as the primary site for reduction reactions. For 4-HPD⁻, the negative charge
15 concentration is located on the nitrogen atom, indicating the site of the reduction reaction.^{44, 45}

16 **Table. 2** Performance comparison of organic electrolyte in aqueous redox flow battery

Electrolyte	Current density	Average CE	D (cm ² /s)	K ₀ (cm/s)	No of cycles	Reference
Anthrarufin / K ₄ [Fe ^{II} (CN) ₆]	20 mA/cm ²	88 %	1.87×10 ⁻⁶	2.63×10 ⁻³	20 cycles	15
Anthraquinone 2-sulfonic acid/ BQDS	8 mA/cm ² (200 mA)	–	3.71×10 ⁻⁶	2.2×10 ⁻⁴	12 cycles	46
Benzoylpyridinium salt/ K ₄ [Fe ^{II} (CN) ₆]	7.85 mA/cm ²	95 %	–	–	10 cycles	8
CDA/ K ₄ [Fe ^{II} (CN) ₆]]	0.04 mA/ cm ²	87 %	5.09 ×10 ⁻⁸	2.66 ×10 ⁻⁴	10 cycles	Present work
	40 mA/ cm ²	98 %			230 cycles	
CDO/ K ₄ [Fe ^{II} (CN) ₆]]	0.04 mA/ cm ²	74 %	5.99 ×10 ⁻⁸	2.26 ×10 ⁻⁴	10 cycles	Present work
	40 mA/ cm ²	96 %			230 cycles	

17

18



1 The deterioration of CDO capacity at the beginning of the charge-discharge cycles is supported
2 by cyclic voltammetry and DFT analysis, as shown in Fig S8. The performance of CDA and
3 CDO is compared with previously published ARFB, as presented in Table. 2. To enhance the
4 efficiency of ARFB, future research should focus on improving the reduction potential,
5 resistance to side reactions and reversible characteristics of CDA and CDO by fine-tuning their
6 molecular structure. In particular, a high conjugated structure is crucial, as it contributes life
7 span and better performance at high current density.

8 Conclusion

9 In this study, we explore the aqueous soluble analytes of CDA and CDO, which share
10 comparably similar molecular weights but are different in heteroatoms pyridone and pyrone.
11 Although they initially display similar charge plateaus, their cyclic stability diverges from the
12 second cycle onward. To unravel their stability in the basic medium and when paired with $K_4[Fe^{II}(CN)_6]$.
13 We utilized CV, revealing stable behavior for CDA- $K_4[Fe^{II}(CN)_6]$ but not for
14 CDO- $K_4[Fe^{II}(CN)_6]$. Their structural characteristics were further analyzed during charging
15 and discharging using 1H -NMR, FTIR spectroscopy and DFT analysis. The results indicate
16 nucleophilic addition in CDO, evidenced by the absence of proton peak in 1H -NMR and FTIR
17 analysis after three charges, which correlates with decreased discharge capacity in subsequent
18 cycles. Additionally, the redox stability of CDA and the deterioration of CDO are supported
19 by HOMO-LUMO energy levels and molecular charge distribution plots. In contrast, CDA
20 exhibits tautomerism in the basic medium, contributing to stable cycling over 17 days. These
21 findings underscore the significant influence of heteroatoms on the stability of ARFB,
22 emphasizing the importance of active sites and heteroatoms in determining stability.

23 Acknowledgements

24 The Author is grateful for the financial support from the National Science and Technology
25 Council (NSTC) of Taiwan, R.O.C., under grant numbers 110-2923-E-007-005, 111-2622-E-
26 011-013, 111-3116-F-011-005, 112-2923-E-007-005, 112-2622-E-011-026, and 112-2221-E-
27 011-013-MY3.

28

29

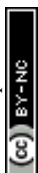


1 References

- 2 1. A. Hollas, X. L. Wei, V. Murugesan, Z. M. Nie, B. Li, D. Reed, J. Liu, V. Sprenkle
3 and W. Wang, *Nat Energy*, 2018, **3**, 508-514.
- 4 2. S. V. Modak, D. Pert, J. L. Tami, W. Shen, I. Abdullahi, X. Huan, A. J. McNeil, B. R.
5 Goldsmith and D. G. Kwabi, *J Am Chem Soc*, 2024, **146**, 5173-5185.
- 6 3. C. Sun and H. Zhang, *ChemSusChem*, 2022, **15**, e202101798.
- 7 4. F. Hasan, V. Mahanta and A. A. A. Abdelazeez, *Adv. Mater. Interfaces*, 2023, **10**.
- 8 5. K. X. Lin, R. Gómez-Bombarelli, E. S. Beh, L. C. Tong, Q. Chen, A. Valle, A.
9 Aspuru-Guzik, M. J. Aziz and R. G. Gordon, *Nat Energy*, 2016, **1**.
- 10 6. D. Hey, R. B. Jethwa, N. L. Farag, B. L. D. Rinkel, E. W. Zhao and C. P. Grey, *Nat*
11 *Commun*, 2023, **14**.
- 12 7. Y. Jing, E. W. Zhao, M. A. Goulet, M. Bahari, E. M. Fell, S. Jin, A. Davoodi, E.
13 Jonsson, M. Wu, C. P. Grey, R. G. Gordon and M. J. Aziz, *Nat Chem*, 2022, **14**,
14 1103-1109.
- 15 8. C. S. Sevov, K. H. Hendriks and M. S. Sanford, *J. Phys. Chem. C*, 2017, **121**, 24376-
16 24380.
- 17 9. B. Yang, L. Hooper-Burkhardt, S. Krishnamoorthy, A. Murali, G. K. S. Prakash and
18 S. R. Narayanan, *J. Electrochem. Soc.*, 2016, **163**, A1442-A1449.
- 19 10. D. C. Crans, M. Mahroof-Tahir, M. D. Johnson, P. C. Wilkins, L. Yang, K. Robbins,
20 A. Johnson, J. A. Alfano, M. E. Godzala, L. T. Austin and G. R. Willsky, *Inorganica*
21 *Chim. Acta*, 2003, **356**, 365-378.
- 22 11. A. Wojciechowska, J. Janczak, K. N. Jarzemska, T. Rojek, A. Gorzsás, Ü. Kersen,
23 T. K. Olszewski and J. Jezierska, *Polyhedron*, 2023, **230**.
- 24 12. E. Avdeeva, E. Shults, T. Rybalova, Y. Reshetov, E. Porokhova, I. Sukhodolo, L.
25 Litvinova, V. Shupletsova, O. Khaziakhmatova, I. Khlusov, A. Guryev and M.
26 Belousov, *Biomolecules*, 2019, **9**.
- 27 13. H. G. Han, Z. X. He, J. L. Liu, Y. Chen and S. Q. Liu, *Ionics*, 2015, **21**, 167-174.
- 28 14. W. Ruan, J. Mao, S. Yang, C. Shi, G. Jia and Q. Chen, *Chem Commun (Camb)*, 2020,
29 **56**, 3171-3174.
- 30 15. C. Mirle, V. Medabalmi and K. Ramanujam, *Catal. Today*, 2021, **370**, 173-180.
- 31 16. K. Lin, R. Gómez-Bombarelli, E. S. Beh, L. Tong, Q. Chen, A. Valle, A. Aspuru-
32 Guzik, M. J. Aziz and R. G. Gordon, *Nat. Energy.*, 2016, **1**, 1-8.



- 1 17. F.-M. Wang, K. Wagari Guji, A. Ramar, L. Merinda and W.-C. Chien, *ACS Sustainable*
2 *Chem. Eng.*, 2021, **9**, 12286-12299. View Article Online
DOI: 10.1039/D4YA00331D
- 3 18. P. Leung, X. H. Li, C. P. de León, L. Berlouis, C. T. J. Low and F. C. Walsh, *Rsc*
4 *Adv*, 2012, **2**, 10125-10156.
- 5 19. H. Wang, S. Y. Sayed, E. J. Lubber, B. C. Olsen, S. M. Shirurkar, S. Venkatakrishnan,
6 U. M. Tefashe, A. K. Farquhar, E. S. Smotkin, R. L. McCreery and J. M. Buriak, *ACS*
7 *Nano*, 2020, **14**, 2575-2584.
- 8 20. M. d. M. Blanco, A. Marcos, M. A. Ruiz, C. Avendano, J. C. Menendez, C. Pedrega
9 and J. M. Pingarron, *Heterocycl. Commun.*, 2000, **6**, 295-300.
- 10 21. X. Yan, L. Zhang, Q. Liu, G. Wang, X. Liu and W. Yang, *Polymer Chemistry*, 2017,
11 **8**, 6356-6361.
- 12 22. H. Thissen, R. A. Evans and V. Ball, *Processes*, 2021, **9**, 82.
- 13 23. M.-A. Goulet, M. Skyllas-Kazacos and E. Kjeang, *Carbon*, 2016, **101**, 390-398.
- 14 24. R. P. Gautam and C. J. Barile, *J. Phy. Chem. C*, 2021, **125**, 8177-8184.
- 15 25. M. Mirzaei, H. Eshtiagh-Hosseini, Z. Karrabi, B. Notash, A. Bauzá Riera and A.
16 Frontera Beccaria, *J. Mol. Struct.*, 2015, vol. 1080, p. 30-36, 2018.
- 17 26. S. Jung, R. Kortlever, R. J. Jones, M. F. Lichterman, T. Agapie, C. C. McCrory and J.
18 C. Peters, *Anal Chem*, 2017, **89**, 581-585.
- 19 27. B. G. Tegegne, D. M. Kabtamu, Y.-Z. Li, Y.-T. Ou, Z.-J. Huang, N.-Y. Hsu, H.-H.
20 Ku, Y.-M. Wang and C.-H. Wang, *J. Energy Storage*, 2023, **61**.
- 21 28. B. G. Tegegne, D. M. Kabtamu, Y.-T. Ou, G.-C. Chen, Z.-J. Huang, N.-Y. Hsu, H.-H.
22 Ku, Y.-M. Wang and C.-H. Wang, *J. Energy Storage*, 2023, **73**.
- 23 29. Z. M. Bhat, R. Thimmappa, M. C. Devendrachari, S. P. Shafi, S. Aralekallu, A. R.
24 Kottaichamy, M. Gautam and M. O. Thotiyl, *J Phys Chem Lett*, 2017, **8**, 3523-3529.
- 25 30. J. J. Kaczur, H. Yang, Z. Liu, S. D. Sajjad and R. I. Masel, *C*, 2020, **6**.
- 26 31. K. Dimos, I. Panagiotopoulos, T. Tsoufis, R. Y. Gengler, A. Moukarika, P. Rudolf,
27 M. A. Karakassides, T. Bakas and D. Gournis, *Langmuir*, 2012, **28**, 10289-10295.
- 28 32. B. Liu, C. W. Tang, H. Jiang, G. Jia and T. Zhao, *J. Power Sources*, 2020, **477**,
29 228985.
- 30 33. G. S. Nambafu, K. Siddharth, C. Zhang, T. Zhao, Q. Chen, K. Amine and M. Shao,
31 *Nano Energy*, 2021, **89**, 106422.
- 32 34. L. C. Jheng, C. Y. Hsu and H. Y. Yeh, *Membranes (Basel)*, 2021, **11**.
- 33 35. G. Das, B. J. Park, J. Kim, D. Kang and H. H. Yoon, *Sci Rep*, 2019, **9**, 9572.
- 34 36. M. G. Marino and K. D. Kreuer, *Chemsuschem*, 2015, **8**, 513-523.



- 1 37. B. Chen, J. Lu, W. Mu, Y. Yang, B. Liu, Y. Yang, H. Wei, S. Peng and X. Li, *J. View Article Online*
2 *Solut. Chem.*, 2022, **51**, 1187-1198. DOI: 10.1039/D4YA00331D
- 3 38. H. B. Schlegel, P. Gund and E. M. Fluder, *J. Am. Chem. Soc.*, 1982, **104**, 5347-5351.
- 4 39. K. Wedege, E. Dražević, D. Konya and A. Bentien, *Scientific reports*, 2016, **6**, 39101.
- 5 40. M. Schuchmann, J. Sonntag and C. Sonntag, *Journal of the Chemical Society, Perkin*
6 *Transactions 2*, 1998, 791-796.
- 7 41. C. Wang, Y. Wang, M. Tao, B. Yu, K. Zhang, J. Wei, Y. Liu, P. Zhang, G. Ding and
8 Z. Tie, *ACS Appl. Energy Mater*, 2022, **5**, 10379-10384.
- 9 42. S. S. Malaganvi, J. Tonannavar Yenagi and J. Tonannavar, *Heliyon*, 2019, **5**, e01586.
- 10 43. P. Kumar and K. K. Dubey, *New and Future Developments in Microbial*
11 *Biotechnology and Bioengineering: Microbial Secondary Metabolites Biochemistry*
12 *and Applications*, 2018, DOI: 10.1016/B978-0-444-63504-4.00013-X, 165-181.
- 13 44. Y. Zhen, C. Zhang, J. Yuan, Y. Zhao and Y. Li, *J. Power Sources*, 2020, **480**, 229132.
- 14 45. C. Mirle and K. Ramanujam, *ACS Appl. Energy Mater*, 2022, **5**, 9711-9721.
- 15 46. B. Yang, L. Hooper-Burkhardt, F. Wang, G. S. Prakash and S. Narayanan, *JES*, 2014,
16 **161**, A1371.
- 17



Data Availability Statement

View Article Online
DOI: 10.1039/D4YA00331D

The data supporting this article have been included as part of the Supplementary Information.

Prof. Fu-Ming Wang (2024.7.26)

